analytical chemistry

pubs.acs.org/ac Article

Ultra-Low Content Bismuth-Anchored Gold Aerogels with Plasmon Property for Enhanced Nonenzymatic Electrochemical Glucose Sensing

Qie Fang, Ying Qin, Hengjia Wang, Weiqing Xu, Hongye Yan, Lei Jiao, Xiaoqian Wei, Jinli Li, Xin Luo, Mingwang Liu, Liuyong Hu, Wenling Gu, and Chengzhou Zhu*

Cite This: *Anal. Chem.* 2022, 94, 11030−11037 Read Online

ACCESS | Metrics & More | Article Recommendations | Supporting Information

ABSTRACT: Effective glucose surveillance provides a strong guarantee for the high-quality development of human health. Au nanomaterials possess compelling applications in nonenzymatic electrochemical glucose biosensors owing to superior catalytic performances and intriguing biocompatibility properties. However, it has been a grand challenge to accurately control the architecture and composition of Au nanomaterials to optimize their optical, electronic, and magnetic properties for further improving the performance of electrocatalytic sensing. Herein, ultra-low content Bi-anchored Au aerogels are synthesized via a one-step reduction strategy. Benefiting from the unique structure of aerogels as well as the synergistic effect between Au and Bi, the optimized $Au_{200}Bi$ aerogels greatly boost the activity of glucose oxidation compared with Au aerogels. Under plasmon resonance excitation, bimetallic $Au_{200}Bi$ aerogels with wider photics-dependent properties further show plasmon-promoted glucose electro-oxidation activity, which is derived from the photothermal and photoelectric effects caused by the local surface plasmon resonance. Thanks to the enhanced performance, a nonenzymatic electrochemical glucose biosensor is constructed to detect glucose with high sensitivity. This plasmon-promoted electrocatalytic activity through the synergetic strategy of bimetallic aerogels has potential applications in various research fields.

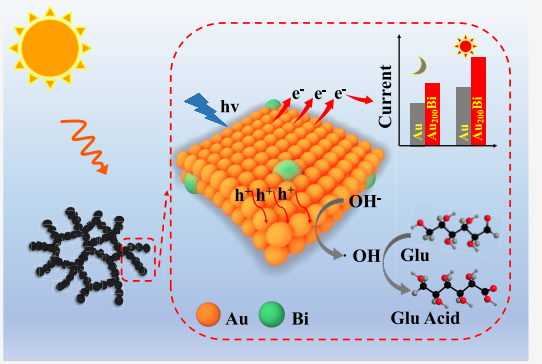

INTRODUCTION

With the booming demands for clinical diagnostic biology, food quality inspection, and pharmaceutical analysis in the era of health, constructing promising sensing platforms to sensitively detect glucose is one of the challenges in the field of sociology and pathology.[1] Au nanomaterials possess great application prospects in nonenzymatic electrochemical glucose sensors due to their superior high catalytic activity and fascinating biocompatibility characteristics.[2−7] However, it has been a grand challenge to rationally design well-tailored Au-based nanomaterials to further boost the electrocatalytic sensing performance. It is well known that architecture, composition, and crystal structure/phase regulating are efficient scenarios for designing high-performance Au nanomaterials.[8−12] Among various noble metal nanomaterials, three-dimensional (3D) nanomaterials possess unique advantages that are formed spontaneously or self-assembled with one-dimensional and two-dimensional nanomaterials.[13,14] Noble metal aerogels (NMAs) as cutting-edge 3D nanomaterials own ultra-low density, large active surface area, porous nanowires structure, and self-supporting characteristics, which have glorious application prospects in electrocatalysis, sensors, and optoelectronics.[15−21] Generally, bimetallic nanomaterials are expected to improve the catalytic performance relative to single metal nanomaterials due to the synergistic effect.[22,23] Especially, the introduction of synergistic components with ultra-low content is an effective and challenging strategy to improve the performance of the catalyst of noble meal aerogels.[22] More importantly, redistributing the electron density of catalysts and optimizing the adsorption energy of the reactant species on the catalyst surface were derived from the strong interactions between ultra-low content metals and metal support, drastically boosting the catalytic performance.[24,25] Synergistically enhanced Au aerogels via doping with ultra-low content metals may hold great promise to serve as advanced catalysts to provide great opportunities for electrocatalytic and sensing performance.

In addition, Au nanostructures possess tunable and fascinating local surface plasmon resonance (LSPR) properties because of the strong absorption of photon energy in the

Received: April 26, 2022
Accepted: July 15, 2022
Published: July 26, 2022

https://doi.org/10.1021/acs.analchem.2c01836
Anal. Chem. 2022, 94, 11030−11037

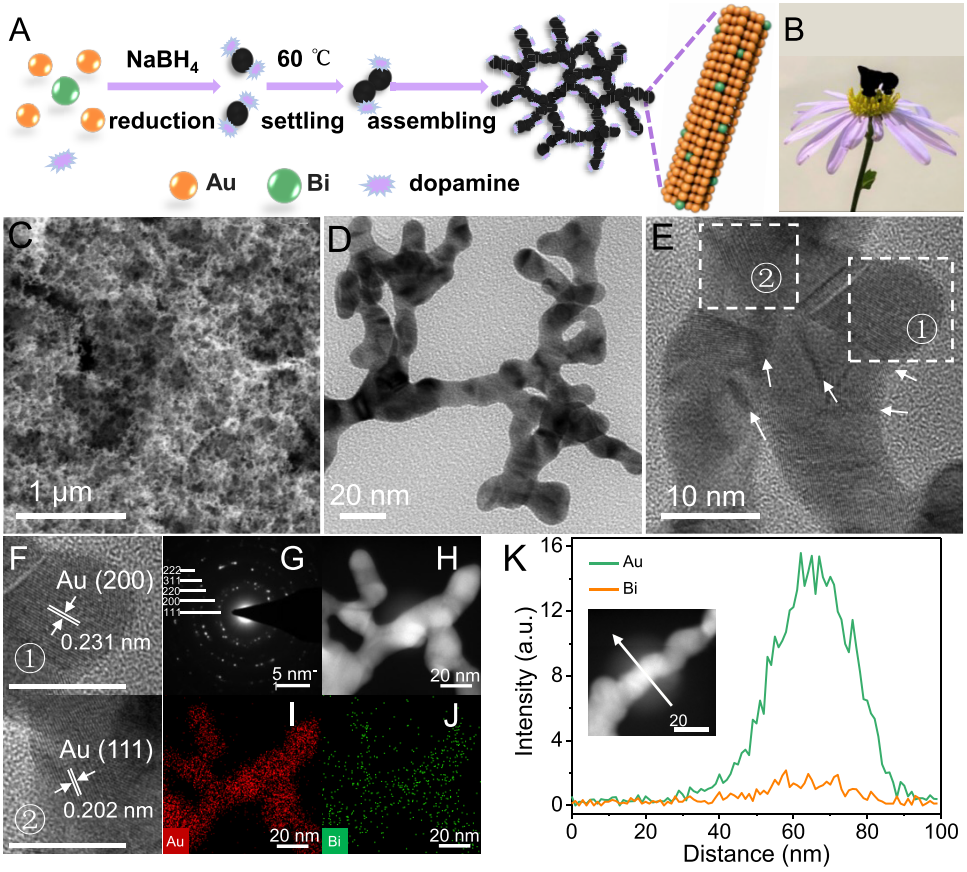

Figure 1. (A) Schematic illustration of the preparation of $Au_{200}Bi$ hydrogels. (B) Digital photo of $Au_{200}Bi$ aerogels. (C) SEM, (D) TEM, (E) HRTEM, (F) enlarged HRTEM images in (E), (G) SAED pattern, (H) HAADF-STEM, and (I, J) corresponding EDX mapping images of $Au_{200}Bi$ aerogels. (K) EDX line scan profiles across the backbone of the inset for $Au_{200}Bi$ aerogels.

ultraviolet−visible region, which can use solar energy to achieve more efficient electric energy conversion.[26−28] LSPR is a unique optical property, which refers to the collective oscillation of internal free electrons in metal nanostructures under light irradiation. The produced hot holes can be eliminated by the oxidation of small molecules owing to the matching of energy levels under suitable voltage bias. This process greatly inhibits the recombination of hot electrons with hot holes, effectively accelerating electrochemical reactions.[29] Without exception, Au-based bimetallic nanomaterials exhibit enhanced electrocatalytic activity by the LSPR effect when exposed to solar energy. For example, Au@Pt core−shell nanoparticles exhibit LSPR-promoted electrocatalytic activity for the methanol oxidation reaction.[30] Additionally, compared to spherical Au nanocrystals, ultrafine Au nanowires exhibit a larger specific surface area and a broader and stronger LSPR.[31] Inspired by this, the plasmon-induced effects provide great potential for Au-based bimetallic aerogels to amplify their specific properties.

Herein, the ultra-low content of Bi as a synergistic component is introduced into the Au aerogels to regulate the electronic structure of Au. The optimized $Au_{200}Bi$ aerogels considerably improve glucose oxidation activity by taking advantage of the unique structure of aerogels as well as the synergistic effect between Au and Bi. During plasmon resonance stimulation, bimetallic $Au_{200}Bi$ aerogels with a wider photics-dependent character further display plasmon-promoted glucose electro-oxidation activity owing to the photothermal and photoelectric effects generated by LSPR. Meanwhile, the quantitative contribution to these two effects was calculated, which is about 10% for the photoelectric effect and 90% for the photothermal effect. Under plasmon resonance, the catalytic mechanism is proposed due to the fact that the generation of plentiful holes on the surface of AuBi aerogels can oxidize the hydroxide to hydroxyl radical (·OH), which further oxidizes glucose at a faster rate. This study demonstrates that plasmon-promoted electrocatalytic activity through a synergetic strategy provides a new perspective to reveal the newly functional enhancement and application potential of noble metal nanomaterials.

RESULTS AND DISCUSSION

As described in Figure 1A, the ultra-low content of Bi-anchored Au hydrogels were successfully synthesized via a one-step reduction strategy induced by dopamine under mild conditions, and its macroscopic aerogels were obtained by a supercritical CO_2 drying technique (Figure 1B). Representative scanning electron microscopy (SEM) and transmission electron microscopy (TEM) images demonstrate the 3D structure of the as-synthesized $Au_{200}Bi$ aerogels, which are composed of interconnected porous and extended nanowire networks with an average diameter of 9.5 nm (Figure 1C,D and Figure S1). The detailed nanostructures were characterized by high-resolution TEM (HRTEM). As marked with white arrows in the HRTEM image (Figure 1E), numerous lattices, grain boundaries, and defects can be observed on the surface of the nanowires, which significantly boost the catalytic efficiency.[32] In the enlarged HRTEM images (Figure 1F), the

https://doi.org/10.1021/acs.analchem.2c01836
Anal. Chem. 2022, 94, 11030−11037

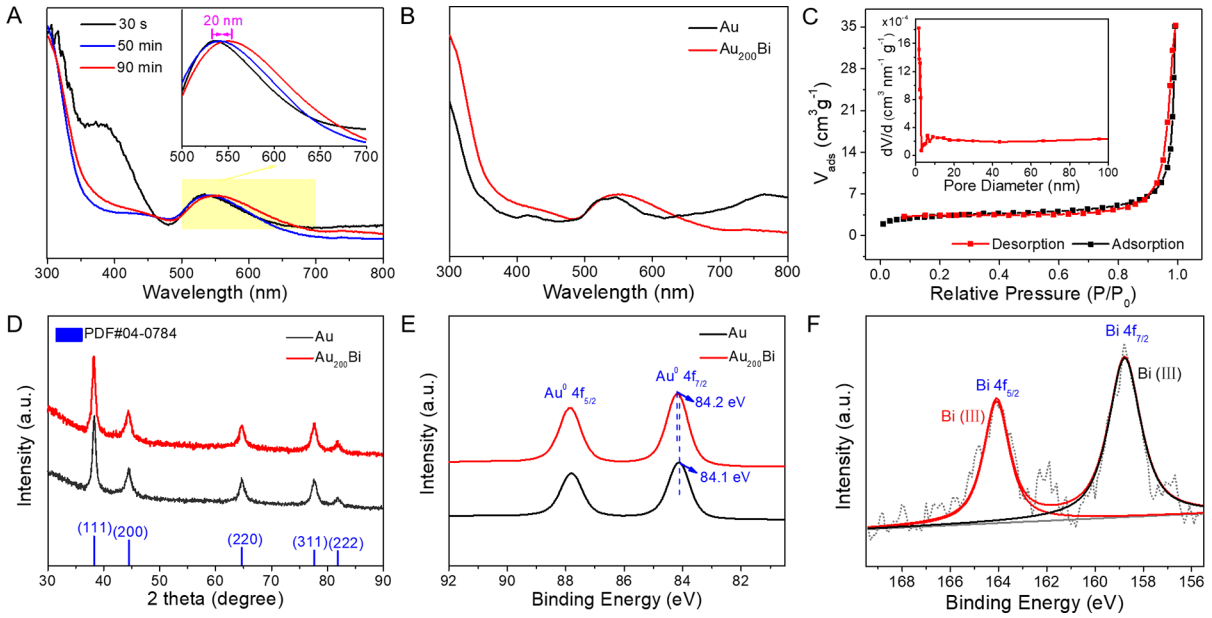

Figure 2. (A) UV−vis spectra for the $Au_{200}Bi$ assembly process at 30 s, 50 min, and 90 min. (B) UV−vis spectra of Au and $Au_{200}Bi$ aerogels. (C) N_2 physisorption isotherm and pore size distribution of $Au_{200}Bi$ aerogels. (D) XRD patterns of Au and $Au_{200}Bi$ aerogels. (E) High-resolution Au 4f XPS spectra of Au and $Au_{200}Bi$ aerogels. (F) High-resolution Bi 4f XPS spectrum of $Au_{200}Bi$ aerogels.

crystal structure with lattice spacings of 0.231 and 0.202 nm can be observed in the $Au_{200}Bi$ aerogels, which were assigned to the (111) and (200) planes of alloyed Au, respectively. Meanwhile, the selected area electron diffraction (SAED) also demonstrates the polycrystalline nature of $Au_{200}Bi$ aerogels assigned to the (111), (200), (220), (311), and (222) planes of Au (Figure 1G). The presence of alloyed features is further verified by high-angle annular dark-field scanning transmission electron microscopy (HAADF-STEM) and energy-dispersive X-ray spectrometry (EDX) elementary analysis (Figure 1H−K), demonstrating the homogeneous distribution of Au and Bi atoms on the entire backbone. It is noted that the content of Bi is considerably lower than that of Au. By simply regulating the molar ratio of metal precursors, the Au, $Au_{100}Bi$, and $Au_{500}Bi$ aerogels were obtained using the same protocol. Their corresponding morphology and size distribution are visualized in Figure S2, both of which reflect 3D nanowire structures and similar sizes. The content of the elements was further detected using inductively coupled plasma optical emission spectrometry (ICP-OES), which is highly consistent with the feed ratio, indicating that the metal precursors are completely reduced (Table S1). Notably, about 0.50% of Bi in the $Au_{200}Bi$ aerogels was detected using ICP-OES, showing exceedingly low Bi content.

To monitor the formation process of $Au_{200}Bi$ aerogels, TEM and UV−vis spectroscopy were employed for supplying evidence of time-dependent growth. As displayed in the corresponding TEM images (Figure S3), the fast growth of $Au_{200}Bi$ hydrogels can be revealed from well-dispersed nanoparticles to small branches and finally assembling into large-scale interconnected networks. Under the driving of gravity, the upper liquid gradually became clear and the product appeared to be gelatinous after 1.5 h.[33] More importantly, the plasmon resonance peak of the $Au_{200}Bi$ colloid was broadened with a redshift from 533 to 553 nm in the process of hydrogel formation (Figure 2A), indicating that more monodisperse nanoparticles self-assembled into aggregated nanoparticle units.[34] It is evident from Figure 2B that the following doping with ultra-low Bi resulted in the redshift of the plasmon band position and an additional considerable broadening, showing that the electrical structure of AuBi differs from that of Au due to the introduction of the ultra-low Bi atom.[35] The specific surface area and pore size distribution of $Au_{200}Bi$ aerogels were measured by nitrogen physisorption isotherms (Figure 2C). The Brunauer−Emmett−Teller surface area of $Au_{200}Bi$ aerogels is 12.40 $m^2\ g^{-1}$. According to the Barrett−Joyner−Halenda theory, the $Au_{200}Bi$ aerogels have typical 3D interlinked porous structure features ranging from micropore, to mesopore, and to macropore. It is well known that the rich specific area and mixed pore structures guarantee the expedited electron/mass transfer process, thereby significantly improving the catalytic activity.[36,37]

To investigate the influence of ultra-low content of Bi doping in promoting glucose oxidation, the crystallographic structures of obtained aerogels were studied by X-ray diffraction (XRD). As shown in Figure 2D and Figure S4, the pure Au aerogels and Au_NBi (N = 100, 200, 500) aerogels with different molar ratios have a typical fcc structure and no additional diffraction peak of Bi is observed. The five diffraction peaks are assigned to the (111), (200), (220), (311), and (222) lattice planes of the Au polycrystalline structure (PDF no. 04-0784),[38] well consistent with the result of the SAED spectrum. After doping Bi atoms, the main diffraction peaks have no obvious shift compared with Au aerogels, manifesting that the ultra-low content of Bi does no effect on the fcc structure of Au. X-ray photoelectron spectroscopy (XPS) was used to investigate the surface chemical information of Au and $Au_{200}Bi$ aerogels. As shown in Figure S5, $Au_{200}Bi$ aerogels consist of Au, Bi, C, O, and N elements. Deconvolution of the XPS spectra via peak fitting shows that the Au $4f_{7/2}$ (83−85 eV) and Au $4f_{5/2}$ (87−89 eV) are attributed to Au^0 species (Figure 2E), indicating the dominant species of metallic Au.[39] Generally, more metal states of noble metal catalysts manifest stronger conductivity

https://doi.org/10.1021/acs.analchem.2c01836
Anal. Chem. 2022, 94, 11030−11037

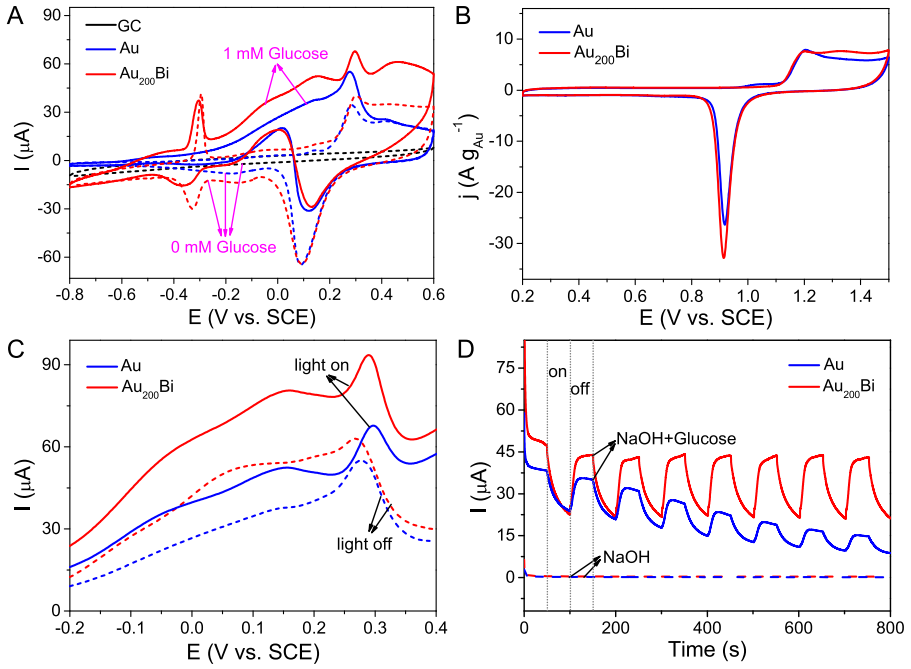

Figure 3. (A) CV curves of the bare glassy carbon (GC) electrode, Au, and $Au_{200}Bi$ electrodes with and without 1 mM glucose. (B) CV curves in the 0.5 M H_2SO_4 solution to determine ECSA. (C) Linear sweep voltammetry (LSV) curves of glucose oxidation with and without illumination (420 nm cut-off light, 200 mW cm^{-2}). (D) Photocurrent responses with and without 1 mM glucose at 0.15 V on the Au and $Au_{200}Bi$ electrodes. Unless otherwise stated, all the above tests were studied in 0.1 M NaOH at a scan rate of 50 mV s^{-1}.

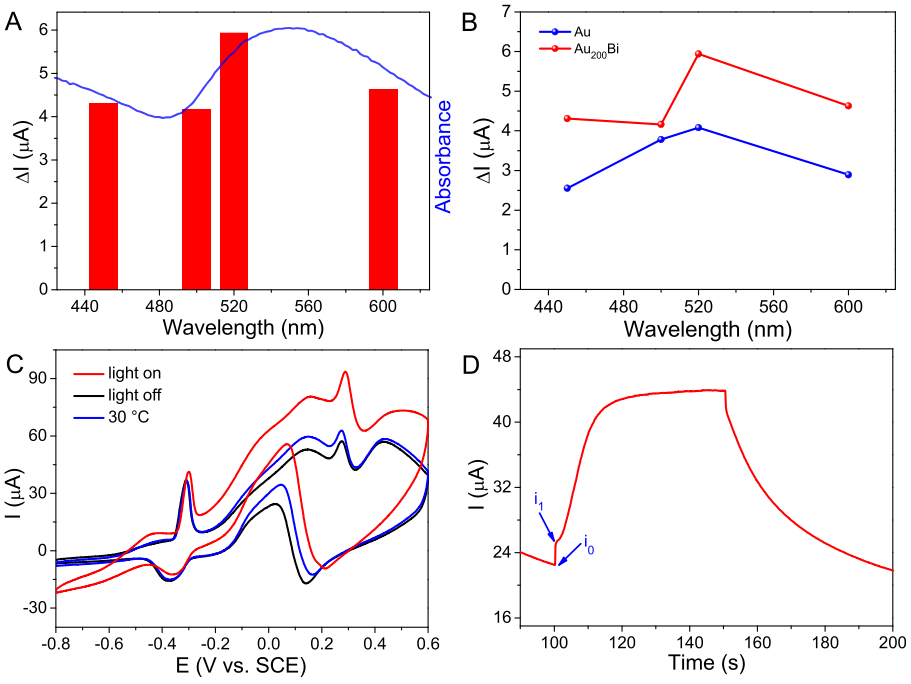

Figure 4. (A) Wavelength-dependent peak current of glucose oxidation (8 mW cm^{-2}) and UV−vis spectra of $Au_{200}Bi$. (B) Increased current values of $Au_{200}Bi$ and Au at different wavelengths at 0.15 V on CV curves. (C) CV curves of light on, light off, and in the dark at 30 °C. (D) *I*−*t* curves of the $Au_{200}Bi$ electrode under illumination with 1 mM glucose at 0.15 V.

and oxidation resistance.[40] Notably, a positive shift in the binding energy of Au results from the interaction between Au and Bi, implying that the electrons tend to transfer from Au atoms to Bi atoms. Such a fluctuant electronic structure of Au is expected to result in the stronger adsorption of reaction intermediates and be a profitable indicator to enhance electrocatalytic performance.[41] In addition, the Bi 4f spectrum in Figure 2F shows two peaks corresponding to Bi $4f_{7/2}$ and Bi $4f_{5/2}$ at 159.1 and 164.4 eV, respectively.[38,42]

The electrocatalytic activity toward glucose oxidation of Au and Au_NBi aerogels was evaluated by using cyclic voltammetry (CV) curves in 0.1 M NaOH solution at a scan rate of 50 mV s^{-1}. Figure 3A displays that the typical oxidation peak starts at about 0.20 V on the Au and $Au_{200}Bi$ electrodes due to the

https://doi.org/10.1021/acs.analchem.2c01836
Anal. Chem. 2022, 94, 11030−11037

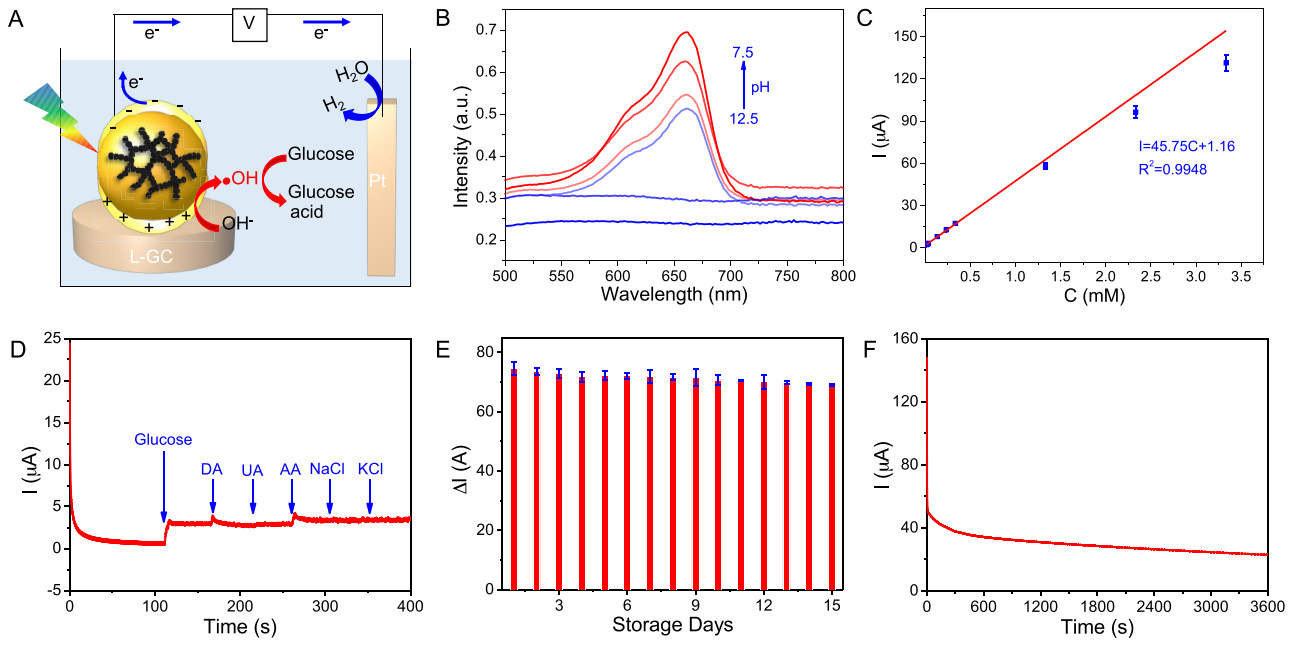

Figure 5. (A) Mechanism of glucose oxidation on $Au_{200}Bi$ aerogels under plasmon excitation. (B) UV−vis spectra of the methylene blue in different pH electrolytes. (C) Calibration curve of current versus glucose concentrations under plasmon excitation. (D) Selectivity, (E) repeatability, and (F) stability of the detection system.

formation of Au oxide that is subsequently reduced. An extra peak at −0.30 V corresponding to the oxidation peak of Bi was detected in Au_NBi aerogels (Figure S6).[43] When 1 mM glucose was added to the electrolyte, significant anodic current peaks attributed to the oxidation of glucose on both Au and Au_NBi electrodes were observed in the positive potential scan. An anodic peak corresponding to the glucose oxidation is found again in the negative potential scan when the oxide layer is reduced. The current of the optimized $Au_{200}Bi$ aerogels is 52.34 μA at a 0.15 V potential, which exhibits a 1.3-fold enhancement of the activity toward glucose oxidation of Au aerogels. The electrochemically active area (ECSA), which is directly connected to catalytic activity, was analyzed to deeply investigate the mechanism of catalytic activity. CV curves were used in a 0.5 M H_2SO_4 solution at a scan rate of 50 mV s^{-1} to determine ECSA of Au and Au_NBi aerogels. A typical reduction peak produced from Au oxide to Au is detected from 0.7 to 1.1 V in Figure 3B and Figure S7. The calculated ECSA values of electrodes modified by Au, $Au_{100}Bi$, $Au_{200}Bi$, and $Au_{500}Bi$ aerogels are 8.49, 8.91, 10.72, and 10.31 $m^2 g_{Au}^{-1}$, respectively. As expected, the $Au_{200}Bi$ aerogels have the highest ECSA, suggesting the most accessible surface area of the catalyst to the electrolyte. Meanwhile, electrochemical impedance spectra (EIS) exhibit that $Au_{200}Bi$ aerogels present a higher conductivity than Au aerogels owing to the smaller charge transfer resistance (Figure S8). These results indicated that ultra-low content Bi plays a critical role in the activity of glucose electro-oxidation, which can be attributed to the advantage of a synergistic effect between components of $Au_{200}Bi$ aerogels.

When the $Au_{200}Bi$ and Au electrodes were illuminated by a 420 nm cut-off light source with an intensity of 200 mW cm^{-2}, a significantly further enhancement of current can be observed in Figure 3C and the corresponding details are shown in Table S2, which is 1.6-fold and 1.4-fold higher than that of the dark condition, respectively. It is noted that the increased activity at 0.15 V potential of the $Au_{200}Bi$ aerogels achieves a 1.8-fold higher value than that of Au aerogels under the plasmon excitation. This result also can be verified from the photocurrent responses of Au and $Au_{200}Bi$ aerogels at a constant potential of 0.15 V (Figure 3D). When plasmon excitation occurs, the anode current increases quickly in the presence of glucose and then falls back rapidly when the light is turned off, whereas the current is almost unchanged in the pure NaOH solution. This phenomenon indicates that the photocurrent response is caused entirely by glucose oxidation. In addition, the plasmon-accelerated glucose oxidation is reversible during continuous switching light irradiation. More importantly, a higher and more stable photocurrent response on the $Au_{200}Bi$ electrode was displayed than that on the Au electrode. Then, the excitation wavelength-dependent currents of glucose oxidation on the Au and $Au_{200}Bi$ aerogels at 0.15 V were measured to gain insight into the plasmon-promoted effect. As shown in Figure 4A and Figure S9, the current changes significantly along with the wavelength and shows a similar trend to the LSPR spectrum of Au and $Au_{200}Bi$ aerogels, respectively. Increased currents at 0.15 V on CV curves over $Au_{200}Bi$ and Au were further measured at different specific wavelengths for comparison (Figure 4B). Notably, $Au_{200}Bi$ exhibits a higher current increment than Au aerogels at a series of different wavelengths, which also supports the fact that the LSPR effect of Au can be optimized via ultra-low Bi doping. In addition, the current density at 0.15 V is proportional to the square root of the scan rate in a linear relationship (Figure S10), implying that electrochemical glucose oxidation is a diffusion-controlled process.

It is known that the excited state electrons in metals relax through electron−phonon coupling to heat the $Au_{200}Bi$ aerogels after plasma excitation, which can further exchange energy with the surrounding medium and thus result in local heating near the $Au_{200}Bi$ aerogels.[44−46] Therefore, the photothermal effect in the electrocatalytic reaction was taken into account. An increased value was shown by assessing the performance toward glucose oxidation of $Au_{200}Bi$ aerogels with

https://doi.org/10.1021/acs.analchem.2c01836
Anal. Chem. 2022, 94, 11030−11037

the increase of temperature (Figure S11), indicating that the photothermal effect caused by LSPR excitation has a positive effect on plasmon-promoted glucose oxidation due to thermally accelerated mass diffusion. In addition, the temperature of the electrolyte is about 30 °C on $Au_{200}Bi$ electrodes under light irradiation conditions (420 nm cut-off light, 200 mW cm^{-2}). Further detailed analysis is demonstrated in Figure 4C; the anodic current under LSPR is higher than that at 30 °C under dark conditions, manifesting that the photothermal and photoelectric effects induced by LSPR are closely associated with the enhanced catalytic activity. This result also can be confirmed by quantitatively calculating the contribution of these two effects to the catalytic activity (Figure 4D). The quantitative contribution to the photoelectric effects was calculated by $(I_1 - I_0)/I_1$.[30,47] which is about 90% for the photothermal effect and 10% for the photoelectric effect (the current after immediate illumination of 0.8 s was designated as I_1, whereas the anodic current before switching on the light at 100 s was designated as I_0). In addition, the electrocatalytic activity increased dramatically with the illumination intensity (Figure S12), which is a characteristic of carriers in a photochemical reaction, indicating the generation of more charge carriers under stronger illumination intensity.

To verify the origin of anode current enhancement under plasmon excitation, the effect of electrolyte pH on the photocurrent response was investigated. As depicted in Figure S13, there is almost no photocurrent response value in the electrolyte of pH 7.5 and 8.5, indicating that the hot holes can hardly directly oxidize glucose. In contrast, the photocurrent gradually increases when the solution pH is from 8.5 to 10.5 and then increases dramatically from 10.5 to 12.5. Based on this result, a plasmon-induced mechanism of glucose oxidation was proposed, which is highly dependent on the ·OH. As illustrated in Figure 5A, electrons oscillate collectively upon LSPR excitation and adsorb enough energy to transfer to active states above the Fermi level of Au. The electron−hole pairs concentrated on the $Au_{200}Bi$ surface due to plasmon-induced charge separation. Under proper voltage bias, the hot holes can be driven to the surface, oxidizing OH^- into ·OH due to the matched energy levels. Then, the strongly oxidizing ·OH diffuses easily through the solution to rapidly oxidize glucose. This process can effectively reduce the recombinational probability of hot electron−hole pairs in the channel. Thereby, more hot electrons are transferred from the surface of $Au_{200}Bi$ aerogels to the external circuit, generating a much larger current. Large quantities of OH^- are easily oxidized to ·OH by hot holes under strongly alkaline conditions.[48] Therefore, hot holes can be more easily obliterated under strongly alkaline conditions than under neutral conditions, resulting in a large photocurrent response. The proposed mechanism was confirmed by detecting ·OH based on the principle that ·OH can degrade and consume methylene blue. As shown in Figure 5B, the wavelength decreases significantly at 650 nm with the increase of electrolyte pH, which was caused by the continuous generation of ·OH and the faster consumption of the methylene blue under strongly alkaline conditions, corresponding with the increased photocurrent response.[49] Since the plasmon effect can accelerate electrochemical reactions and cause an enhancement in performance, chemical or biological sensors based on plasmon excitation should have unparalleled advantages, including high sensitivity and low detection limit.

Thus, as a proof of concept, a nonenzymatic electrochemical glucose biosensor was constructed based on synergistic enhancement and the plasmon resonance effect. The amperometric detection of glucose under plasmon excitation was conducted on $Au_{200}Bi$ aerogels at 0.15 V in 0.1 M NaOH, and the corresponding calibration curve is shown in Figure 5C. The linear range is 13 μM−3.3 mM with a sensitivity of 664 μA mM^{-1} cm^{-2}, and the detection limit is 8.7 μM (signal-to-noise ratio of 3). Due to high current density, $Au_{200}Bi$ aerogels can support proper detection ability at a low concentration range, suggesting that the electrical analysis sensor of the Au aerogel system integrated with the synergistic enhancement and plasmon resonance has a great prospect in the practical application of glucose. In the case of a practical biosensor, selectivity should be given considerably greater consideration. A variety of interfering species, including dopamine (DA), uric acid (UA), ascorbic acid (AA), Na^+, and K^+ were employed to display the selectivity of the constructed nonenzymatic glucose sensing platform. Figure 5D demonstrates the chronoamperometric measurements of $Au_{200}Bi$ at 0.15 V in 0.1 M NaOH with successive addition of 1 mM glucose and 0.25 mM various interfering species and shows the good selectivity of the nonenzymatic glucose sensor that was fabricated. As illustrated in Figure 5E, the fabricated nonenzymatic glucose sensor showcases satisfactory repeatability with a relative standard deviation of less than 2.8%. Similarly, the repeatability was performed in five separate sensors with a relative standard deviation of less than 3.0% (Figure S14), manifesting the satisfactory reproducibility of $Au_{200}Bi$. Significantly, $Au_{200}Bi$ aerogels also show superior glucose detection performance in terms of detection limit and sensitivity compared with those previously reported (Table S3).

Additionally, there are virtually no fluctuations in current throughout the long-term test for $Au_{200}Bi$ in Figure 5F, demonstrating their remarkable stability. Furthermore, no noticeable changes are found in the TEM image (Figure S15), XRD pattern (Figure S16), and high-resolution XPS spectra (Figure S17) of the sample after the 3600 s stability tests, demonstrating the strong endurance of the $Au_{200}Bi$ aerogels as well. The plasmon-promoted electrochemical oxidation reaction and ultra-low content Bi doping endowed Au aerogels with enhanced electrochemical signals for nonenzymatic electrochemical glucose detection with high sensitivity and stability. This insight opens new horizons for the construction of nonenzymatic electrochemical glucose sensors based on a synergetic strategy and the plasmon effect.

CONCLUSIONS

In summary, ultra-low content Bi-anchored Au aerogels were synthesized via a dopamine-induced one-step reduced method. Using glucose electrocatalysis as a model system, the origin of the accelerated glucose oxidation was investigated. Compared with Au aerogels, the optimized $Au_{200}Bi$ aerogels greatly boost the activity of glucose oxidation owing to the unique structure of AuBi aerogels as well as the synergistic effect between Au and Bi. Under plasmon resonance excitation, bimetallic $Au_{200}Bi$ aerogels with a wider photics-dependent character further display plasmon-promoted glucose electro-oxidation activity owing to the photothermal and photoelectric effects generated by LSPR. Meanwhile, the quantitative contribution of the ratio of these two effects toward the catalytic activity was calculated, which is about 90% for the photothermal effect and 10% for the photoelectric effect. Interestingly, anodic currents vary

https://doi.org/10.1021/acs.analchem.2c01836
Anal. Chem. 2022, 94, 11030−11037

greatly under strongly alkaline conditions, which arise from the faster capture of hot holes using abundant hydroxyl. Furthermore, the nonenzymatic electrochemical glucose sensor based on $Au_{200}Bi$ with a plasmon property shows high sensitivity and stability. This work endeavor sheds light on a rational design of highly active nanomaterials for catalytic signal amplification in sensing and biosensing applications.

EXPERIMENTAL SECTION

Synthesis of AuBi Hydrogels/Aerogels. Typically, $NaBH_4$ (2 mL, 0.05 M) was fleetly introduced to a 30 mL solution that contains $HAuCl_4$ (1.3 mM), $Bi(NO_3)_3$ (0.0067 mM), and dopamine (0.083 mg/mL) under stirring at 60 °C for 15 s and then settled at the temperature. After about 1.5 h, $Au_{200}Bi$ hydrogels were generated at the bottom of the vial. Then, carefully washing with water three times and replacing the supernatant with acetone, $Au_{200}Bi$ aerogels could be obtained from supercritical CO_2 drying. Furthermore, $Au_{100}Bi$, $Au_{500}Bi$, and Au aerogels were obtained via a method similar to that above by changing the content of Bi precursors.

Electrochemical Measurements. For the glucose oxidation reaction, 5 μL of the as-obtained aerogel aqueous solution was dropped on the surface of the GC electrode and dried at 50 °C followed by dropping 3 μL of Nafion (0.05%) and drying at 50 °C.

ASSOCIATED CONTENT

Supporting Information

The Supporting Information is available free of charge at https://pubs.acs.org/doi/10.1021/acs.analchem.2c01836.

Additional experimental details; characterization of Au, $Au_{100}Bi$, $Au_{200}Bi$, and $Au_{500}Bi$; glucose oxidation performance of AuBi aerogel with different mole ratios; EIS spectra; wavelength-dependence peak current and UV−vis spectra of Au aerogels; effects of scan rate, temperature, irradiation intensity, and pH on electrocatalytic oxidation of glucose; characterization of $Au_{200}Bi$ after stability; the results by ICP-OES; and detailed data from electrochemical tests (PDF)

AUTHOR INFORMATION

Corresponding Author

Chengzhou Zhu − *Key Laboratory of Pesticides and Chemical Biology of Ministry of Education, International Joint Research Center for Intelligent Biosensing Technology and Health, College of Chemistry, Central China Normal University, Wuhan 430079, P.R. China;* orcid.org/0000-0003-0679-7965; Email: czzhu@ccnu.edu.cn

Authors

Qie Fang − *Key Laboratory of Pesticides and Chemical Biology of Ministry of Education, International Joint Research Center for Intelligent Biosensing Technology and Health, College of Chemistry, Central China Normal University, Wuhan 430079, P.R. China*

Ying Qin − *Key Laboratory of Pesticides and Chemical Biology of Ministry of Education, International Joint Research Center for Intelligent Biosensing Technology and Health, College of Chemistry, Central China Normal University, Wuhan 430079, P.R. China*

Hengjia Wang − *Key Laboratory of Pesticides and Chemical Biology of Ministry of Education, International Joint Research Center for Intelligent Biosensing Technology and Health, College of Chemistry, Central China Normal University, Wuhan 430079, P.R. China*

Weiqing Xu − *Key Laboratory of Pesticides and Chemical Biology of Ministry of Education, International Joint Research Center for Intelligent Biosensing Technology and Health, College of Chemistry, Central China Normal University, Wuhan 430079, P.R. China*

Hongye Yan − *Key Laboratory of Pesticides and Chemical Biology of Ministry of Education, International Joint Research Center for Intelligent Biosensing Technology and Health, College of Chemistry, Central China Normal University, Wuhan 430079, P.R. China*

Lei Jiao − *Key Laboratory of Pesticides and Chemical Biology of Ministry of Education, International Joint Research Center for Intelligent Biosensing Technology and Health, College of Chemistry, Central China Normal University, Wuhan 430079, P.R. China*

Xiaoqian Wei − *Key Laboratory of Pesticides and Chemical Biology of Ministry of Education, International Joint Research Center for Intelligent Biosensing Technology and Health, College of Chemistry, Central China Normal University, Wuhan 430079, P.R. China*

Jinli Li − *Key Laboratory of Pesticides and Chemical Biology of Ministry of Education, International Joint Research Center for Intelligent Biosensing Technology and Health, College of Chemistry, Central China Normal University, Wuhan 430079, P.R. China*

Xin Luo − *Key Laboratory of Pesticides and Chemical Biology of Ministry of Education, International Joint Research Center for Intelligent Biosensing Technology and Health, College of Chemistry, Central China Normal University, Wuhan 430079, P.R. China*

Mingwang Liu − *Key Laboratory of Pesticides and Chemical Biology of Ministry of Education, International Joint Research Center for Intelligent Biosensing Technology and Health, College of Chemistry, Central China Normal University, Wuhan 430079, P.R. China*

Liuyong Hu − *Hubei Key Laboratory of Plasma Chemistry and Advanced Materials, Hubei Engineering Technology Research Center of Optoelectronic and New Energy Materials, Wuhan Institute of Technology, Wuhan 430205, P. R. China*

Wenling Gu − *Key Laboratory of Pesticides and Chemical Biology of Ministry of Education, International Joint Research Center for Intelligent Biosensing Technology and Health, College of Chemistry, Central China Normal University, Wuhan 430079, P.R. China*

Complete contact information is available at: https://pubs.acs.org/10.1021/acs.analchem.2c01836

Notes

The authors declare no competing financial interest.

ACKNOWLEDGMENTS

The authors gratefully acknowledge the financial support by self-determined research funds of CCNU from the colleges' basic research and operation of MOE (CCNU20TS013 and CCNU20QN007), and the Program of Introducing Talents of Discipline to Universities of China (111 programs, B17019).

REFERENCES

(1) Wang, J. *Chem. Rev.* **2008**, *108*, 814−825.

(2) Xie, F.; Huang, Z.; Chen, C.; Xie, Q.; Huang, Y.; Qin, C.; Liu, Y.; Su, Z.; Yao, S. *Electrochem. Commun.* **2012**, *18*, 108−111.
(3) Song, Y.; Zhu, C.; Li, H.; Du, D.; Lin, Y. *RSC Adv.* **2015**, *5*, 82617−82622.
(4) Lim, H.; Kim, J.; Kani, K.; Masud, M. K.; Park, H.; Kim, M.; Alsheri, S. M.; Ahamad, T.; Alhokbany, N.; Na, J.; Malgras, V.; Bando, Y.; Yamauchi, Y. *Small* **2020**, *16*, 1902934.
(5) Shim, K.; Kim, J.; Shahabuddin, M.; Yamauchi, Y.; Hossain, M. S. A.; Kim, J. H. *Sens. Actuators, B* **2018**, *255*, 2800−2808.
(6) Masud, M. K.; Na, J.; Lin, T.-E.; Malgras, V.; Preet, A.; Ibn Sina, A. A.; Wood, K.; Billah, M.; Kim, J.; You, J.; Kani, K.; Whitten, A. E.; Salomon, C.; Nguyen, N.-T.; Shiddiky, M. J. A.; Trau, M.; Hossain, M. S. A.; Yamauchi, Y. *Biosens. Bioelectron.* **2020**, *168*, No. 112429.
(7) Shim, K.; Wang, Z.-L.; Mou, T. H.; Bando, Y.; Alshehri, A. A.; Kim, J.; Hossain, M. S. A.; Yamauchi, Y.; Kim, J. H. *ChemPlusChem* **2018**, *83*, 401−406.
(8) Alivisatos, A. P. *Science* **1996**, *271*, 933.
(9) Daniel, M.-C.; Astruc, D. *Chem. Rev.* **2004**, *104*, 293−346.
(10) Sun, X.; Dong, S.; Wang, E. *Angew. Chem., Int. Ed.* **2004**, *43*, 6360−6363.
(11) Song, C.; Zhao, G.; Zhang, P.; Rosi, N. L. *J. Am. Chem. Soc.* **2010**, *132*, 14033−14035.
(12) Ma, Y.; Kuang, Q.; Jiang, Z.; Xie, Z.; Huang, R.; Zheng, L. *Angew. Chem., Int. Ed.* **2008**, *47*, 8901−8904.
(13) Wang, L.; Yang, H.; Shu, T.; Chen, X.; Huang, Y.; Hu, X. *ChemElectroChem* **2017**, *4*, 2428−2441.
(14) Bao, Y.; Feng, L. *Acta Phys.-Chim. Sin.* **2021**, *37*, 2008031.
(15) Du, R.; Joswig, J.-O.; Hübner, R.; Zhou, L.; Wei, W.; Hu, Y.; Eychmüller, A. *Angew. Chem., Int. Ed.* **2020**, *59*, 8293−8300.
(16) Fang, Q.; Wang, H.; Lv, X.; Wei, X.; Luo, X.; Huang, J.; Jiao, L.; Gu, W.; Song, W.; Zhu, C. *ACS Sustainable Chem. Eng.* **2021**, *9*, 13039−13046.
(17) Shi, Q.; Zhu, C.; Li, Y.; Xia, H.; Engelhard, M. H.; Fu, S.; Du, D.; Lin, Y. *Chem. Mater.* **2016**, *28*, 7928−7934.
(18) Wang, H.; Fang, Q.; Gu, W.; Du, D.; Lin, Y.; Zhu, C. *ACS Appl. Mater. Interfaces* **2020**, *12*, 52234−52250.
(19) Jiao, L.; Xu, W.; Yan, H.; Wu, Y.; Gu, W.; Li, H.; Du, D.; Lin, Y.; Zhu, C. *Chem. Commun.* **2019**, *55*, 9865−9868.
(20) Wu, Y.; Jiao, L.; Xu, W.; Gu, W.; Zhu, C.; Du, D.; Lin, Y. *Small* **2019**, *15*, 1900632.
(21) Huang, J.; Jiao, L.; Xu, W.; Fang, Q.; Wang, H.; Cai, X.; Yan, H.; Gu, W.; Zhu, C. *ACS Appl. Mater. Interfaces* **2021**, *13*, 33383−33391.
(22) Zhu, C.; Shi, Q.; Fu, S.; Song, J.; Xia, H.; Du, D.; Lin, Y. *Adv. Mater.* **2016**, *28*, 8779−8783.
(23) Huang, H.; Li, K.; Chen, Z.; Luo, L.; Gu, Y.; Zhang, D.; Ma, C.; Si, R.; Yang, J.; Peng, Z.; Zeng, J. *J. Am. Chem. Soc.* **2017**, *139*, 8152−8159.
(24) Wang, H.; Jiao, L.; Zheng, L.; Fang, Q.; Qin, Y.; Luo, X.; Wei, X.; Hu, L.; Gu, W.; Wen, J.; Zhu, C. *Adv. Funct. Mater.* **2021**, *31*, 2103465.
(25) Dubale, A. A.; Zheng, Y.; Wang, H.; Hübner, R.; Li, Y.; Yang, J.; Zhang, J.; Sethi, N. K.; He, L.; Zheng, Z.; Liu, W. *Angew. Chem., Int. Ed.* **2020**, *59*, 13891−13899.
(26) Linic, S.; Christopher, P.; Ingram, D. B. *Nat. Mater.* **2011**, *10*, 911−921.
(27) Chavez, S.; Aslam, U.; Linic, S. *ACS Energy Lett.* **2018**, *3*, 1590−1596.
(28) Yu, S.; Kim, Y. H.; Lee, S. Y.; Song, H. D.; Yi, J. *Angew. Chem., Int. Ed.* **2014**, *53*, 11203−11207.
(29) Shang, B.; Cui, X.; Jiao, L.; Qi, K.; Wang, Y.; Fan, J.; Yue, Y.; Wang, H.; Bao, Q.; Fan, X.; Wei, S.; Song, W.; Cheng, Z.; Guo, S.; Zheng, W. *Nano Lett.* **2019**, *19*, 2758−2764.
(30) Yang, H.; He, L.-Q.; Hu, Y.-W.; Lu, X.; Li, G.-R.; Liu, B.; Ren, B.; Tong, Y.; Fang, P.-P. *Angew. Chem., Int. Ed.* **2015**, *54*, 11462−11466.
(31) Takahata, R.; Yamazoe, S.; Koyasu, K.; Tsukuda, T. *J. Am. Chem. Soc.* **2014**, *136*, 8489−8491.
(32) Shi, Q.; Zhu, C.; Zhong, H.; Su, D.; Li, N.; Engelhard, M. H.; Xia, H.; Zhang, Q.; Feng, S.; Beckman, S. P.; Du, D.; Lin, Y. *ACS Energy Lett.* **2018**, *3*, 2038−2044.
(33) Du, R.; Hu, Y.; Hübner, R.; Joswig, J.-O.; Fan, X.; Schneider, K.; Eychmüller, A. *Sci. Adv.* **2019**, *5*, No. eaaw4590.
(34) El-Sayed, M. A. *Acc. Chem. Res.* **2001**, *34*, 257−264.
(35) Zhang, X.; Fan, Y.; You, E.; Li, Z.; Dong, Y.; Chen, L.; Yang, Y.; Xie, Z.; Kuang, Q.; Zheng, L. *Nano Energy* **2021**, *84*, No. 105950.
(36) Du, R.; Jin, X.; Hübner, R.; Fan, X.; Hu, Y.; Eychmüller, A. *Adv. Energy Mater.* **2020**, *10*, 1901945.
(37) Jiang, X.; Du, R.; Hübner, R.; Hu, Y.; Eychmüller, A. *Matter* **2021**, *4*, 54−94.
(38) Yan, H.; Jiao, L.; Wang, H.; Zhu, Y.; Chen, Y.; Shuai, L.; Gu, M.; Qiu, M.; Gu, W.; Zhu, C. *Sens. Actuators, B* **2021**, *343*, No. 130108.
(39) Zhao, W.; Gonzaga, F.; Li, Y.; Brook, M. A. *Adv. Mater.* **2007**, *19*, 1766−1771.
(40) Chen, L.; Lu, L.; Zhu, H.; Chen, Y.; Huang, Y.; Li, Y.; Wang, L. *Nat. Commun.* **2017**, *8*, 14136.
(41) Yang, X.; Liang, Z.; Chen, S.; Ma, M.; Wang, Q.; Tong, X.; Zhang, Q.; Ye, J.; Gu, L.; Yang, N. *Small* **2020**, *16*, 2004727.
(42) Li, H.; Hu, T.; Liu, J.; Song, S.; Du, N.; Zhang, R.; Hou, W. *Appl. Catal., B* **2016**, *182*, 431−438.
(43) Zalineeva, A.; Serov, A.; Padilla, M.; Martinez, U.; Artyushkova, K.; Baranton, S.; Coutanceau, C.; Atanassov, P. B. *J. Am. Chem. Soc.* **2014**, *136*, 3937−3945.
(44) Kale, M. J.; Avanesian, T.; Christopher, P. *ACS Catal.* **2014**, *4*, 116−128.
(45) Linic, S.; Aslam, U.; Boerigter, C.; Morabito, M. *Nat. Mater.* **2015**, *14*, 744−744.
(46) Christopher, P.; Xin, H.; Linic, S. *Nat. Chem.* **2011**, *3*, 467−472.
(47) Yang, H.; Wang, Z.-H.; Zheng, Y.-Y.; He, L.-Q.; Zhan, C.; Lu, X.; Tian, Z.-Q.; Fang, P.-P.; Tong, Y. *J. Am. Chem. Soc.* **2016**, *138*, 16204−16207.
(48) Simon, T.; Bouchonville, N.; Berr, M. J.; Vaneski, A.; Adrović, A.; Volbers, D.; Wyrwich, R.; Döblinger, M.; Susha, A. S.; Rogach, A. L.; Jäckel, F.; Stolarczyk, J. K.; Feldmann, J. *Nat. Mater.* **2014**, *13*, 1013−1018.
(49) Satoh, A. Y.; Trosko, J. E.; Masten, S. J. *Environ. Sci. Technol.* **2007**, *41*, 2881−2887.

https://doi.org/10.1021/acs.analchem.2c01836
Anal. Chem. 2022, 94, 11030−11037